17th AIAA International Space Planes and Hypersonic Systems and Technologies Conference
11 - 14 April 2011, San Francisco, California

AIAA 2011-2394

Uncertainty Propagation in Integrated Airframe-Propulsion System Analysis for Hypersonic Vehicles

Nicolas Lamorte*, Peretz P. Friedmann†, Derek J. Dalle‡, Sean M. Torrez§ and James F. Driscoll¶

Department of Aerospace Engineering

University of Michigan

1320 Beal Ave.

Ann Arbor, Michigan 48109–2140

Ph : (734) 763-2354 Fax : (734) 763-0578

Email: peretzf@umich.edu

Air–breathing hypersonic vehicles are based on airframe–integrated SCRAMjet engine. The elongated forebody which serves as the inlet of the engine is subject to harsh aerothermodynamic loading which causes it to deform. Unpredicted deformations may produce unstart, combustor chocking or structural failure due to increased loads. This study presents a framework allowing one to assess the impact of aerothermoelastic deformations on the engine performance prediction. Aerothermoelastic deformations are calculated for trajectories and angle of attack and transferred to a SCRAMjet engine analysis. Uncertainty associated with deformation prediction is propagated to the engine performance analysis. The importance of modeling the aerodynamic heating and aerothermoelastic deformations at the cowl of the inlet is noted. The cowl deformation is the main contributor to uncertainty and sensitivity of the propulsion system analysis.

Nomenclature

c_p	Specific heat of air
c	Specific heat of material
E	Young's modulus
ER	$= \left(\frac{\dot{m}_f}{\dot{m}_{4,O_2}}\right) / \left(\frac{\dot{m}_f}{\dot{m}_{4,0_2}}\right)_{st}$, Equivalence ratio
$f(\xi)$	Output of interest
F_x	Force acting in the $x-$direction
H	Altitude
h	Coordinate across the thickness of the skin
h_1, h_2	Thickness of the TPS layers
h_3	Thickness of the structural layer
k	Thermal conductivity
M	Mach number
$\dot{m}_{air}$	Air mass flow rate
$\dot{m}_f$	Fuel mass flow rate
m_f	Expected value of f
P	Pressure

*Graduate Research Assistant, Student Member, AIAA
†François-Xavier Bagnoud Professor, Fellow, AIAA
‡Graduate Research Assistant, Student Member, AIAA
§Graduate Research Assistant, Student Member, AIAA
¶Professor of Aerospace Engineering, Fellow, AIAA.

q_{aero}	Aerodynamic heat flux
q	Dynamic pressure
Re	Reynolds number based on a length of 1 m
t	Flight time
T	Temperature
T_r	Recovery temperature
u	Axial displacement at elastic axis
w	Transverse displacement
w_j	weight in numerical integration
(x', y', z')	Coordinate system for the corrugated panel
x	Coordinate along vehicle, from leading edge, positive aft
y	Coordinate in the spanwise direction, from centerline of the vehicle
z	Coordinate normal to vehicle, from leading edge point, positive up

Greek Symbols

α	Angle of attack
α_f	Angle of attack of the trajectory
α_T	Thermal expansion coefficient
$\gamma = \frac{c_p}{c_v}$	Specific heat ratio
ϵ	Emissivity
ν	Poisson ratio
ξ_1, ξ_2	Uncertain variables
ρ	Density of air
ρ_M	Density of material
σ_f	Standard deviation of f
ϕ_j	Interpolation function

Subscripts

∞	Freestream condition
0	Total condition
4	Condition at the exit of the combustor
i	Initial value
st	Stoichiometric condition
$wall$	At the wall

I. Introduction

RESEARCH on hypersonic vehicles is motivated by military and civilian applications such as unmanned rapid response to threats and reusable launch vehicles for affordable access to space.[1–7] Such vehicles are based on lifting body designs with a tightly integrated airframe and propulsion system. For sustained hypersonic cruise speeds, air–breathing engines are needed. Accurate modeling of propulsion system is critical to hypersonic vehicle performance, stability, and reliability analyses. Flight at hypersonic speeds within the atmosphere produces severe aerodynamic heating which may cause vehicle failure. Aerothermoelastic deformations can interact with the propulsion system.[7–10] Furthermore, hypersonic flight conditions produce high levels of aerodynamic heat flux, shock interactions, viscous interactions, dissociations and chemically reacting flow.[11,12] Validation of a fully coupled aerothermoelastic–propulsive system is not feasible due to scaling effects and lack of suitable wind tunnels.[13] Therefore development of hypersonic vehicles requires a degree of confidence in computational results which cannot be fully validated in ground test facilities.[4] The structure of the flow in the inlet is experimentally studied only for short durations for a given flight condition.[14,15] Aerothermoelastic deformations are neglected. Shocks, expansion fans, boundary layers, detachment and reattachment regions and their interactions at the inlet are complex and computationally expensive to predict. Therefore, comprehensive analysis codes must employ computationally efficient models based on simplifying assumptions of the physics and/or reduced-order modeling of full order computations. Due to the critical role of simulation codes in hypersonic vehicle analysis, the importance of quantifying the

risk/reliability in such computational simulations is particularly important.

Modeling the aero–thermo–elastic–propulsion interactions, even for a simple geometry of a typical hypersonic vehicle, requires several simplifying assumptions in each component of the analysis.[7,16] Simplified models are computationally efficient and enable comprehensive analysis of a hypersonic vehicle in a control–oriented or optimization–oriented framework. To compensate for unmodeled physics and simplifications, an uncertainty propagation approach is used to quantify sensitivity, robustness and reliability of a given configuration with respect to identified uncertainties.[16,17] The simplifying assumptions, such as fixed geometry or the neglect of real gas effects introduce uncertainty which affects the reliability of the analysis. For this class of problems the uncertainty due to both unmodeled physics and the need to use approximate or reduced order models (ROM) for several components, must be propagated through the analysis.

The most effective approaches for propagating uncertainty in aeroelastic problems are direct Monte Carlo simulations (MCS) and response surface based methods such as stochastic collocation (SC) or polynomial chaos expansion (PCE). In this study, SC is considered as an effective alternative to direct MCS which has prohibitive computational costs for complex problems. The SC approach was shown to outperform PCE in a recent study[18] and was successfully used to propagate uncertainty in aeroelastic and aerothermoelastic analyses of hypersonic vehicle.[19] In Ref. 16, the effect of uncertainty associated with the use of approximate models in the analysis of the propulsion system of a hypersonic vehicle is propagated to the net thrust as a function of fuel inflow rate for two fixed configurations using MCS. Error associated with the approximate models have a significant impact on the prediction of the thrust. Previous studies showed that aeroelastic deformation of the inlet have a significant impact on the performance of the engine.[8]

Only a limited number of air–breathing hypersonic vehicles have flown. Among them the X–43 and more recently the X–51 are representative vehicles of air–breathing hypersonic aircraft concepts, depicted in Fig. 1.

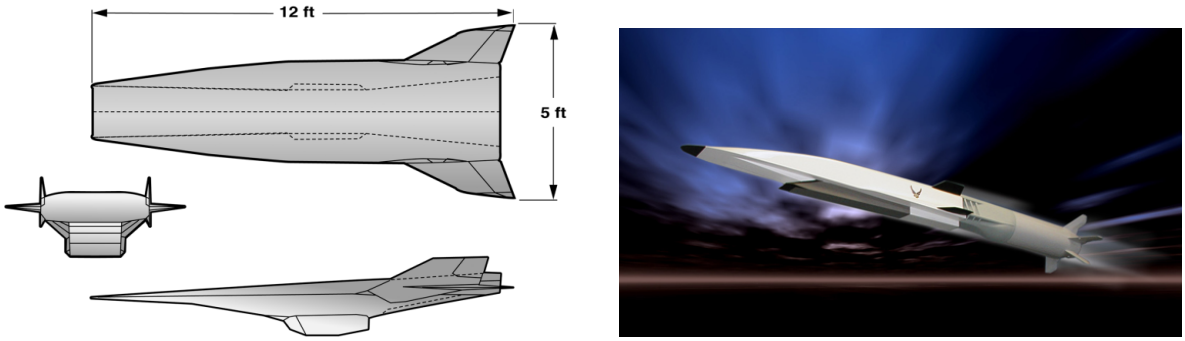

(a) X–43 (b) X–51

Figure 1. Hypersonic vehicles

Short duration and long duration flights introduce different aerothermoelastic issues. The overall objective of this study is to quantify the effect of variations in geometry due to thermal expansion/stresses and aerodynamic loading in an integrated airframe propulsion system analysis for a hypersonic vehicle. It is expected that this study will serve as a guide towards understanding and quantifying uncertainty in studies of integrated aerothermoelastic–propulsion system of air–breathing vehicle, as well as overall vehicle behavior or design.

The specific goals of this study are:

1. Evaluate aerothermoelastic deformations of the main components of the flow path of the engine of a typical hypersonic vehicle: inlet, cowl and nozzle.

2. Analyze the stability of the propulsion system in a probabilistic manner in order to quantify the risk/reliability associated with uncertainty in the predicted aerothermoelastic deformations.

The following section describes the 2D aerothermoelastic analysis and engine analysis of a generic hypersonic vehicle. The prediction of aerothermoelastic propulsive effects on the engine requires four different analysis capabilities: a propulsion model with deforming geometry capability, a structural model with

temperature–dependent material properties, an aerodynamic analysis capable of predicting heat transfer of external hypersonic flow over a surface and a heat transfer analysis.

II. General Hypersonic Vehicle Modeling

The aerothermoelastic analysis of a typical hypersonic analysis is illustrated by the flow chart in Fig. 2.

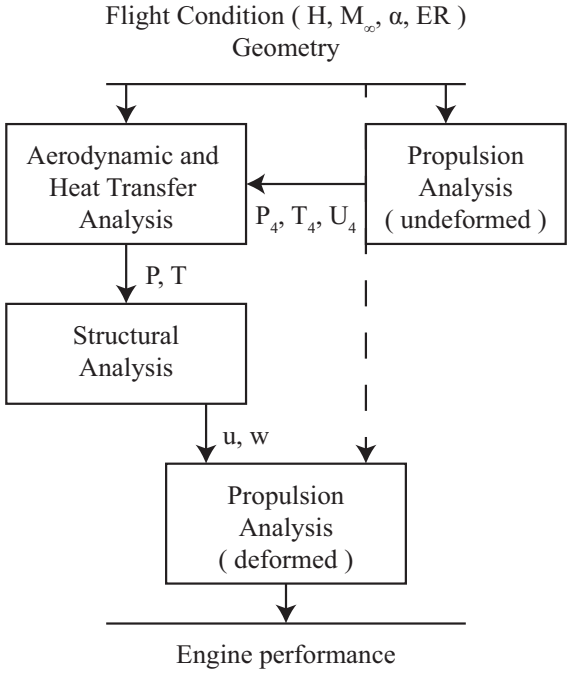

Figure 2. Modeling flow chart

A flight condition is determined by the altitude, H, the Mach number M_∞, the angle of attack of the vehicle, α, which determines the freestream conditions; and the equivalence ratio, $ER = \left(\frac{\dot{m}_f}{\dot{m}_{O_2,4}}\right) / \left(\frac{\dot{m}_f}{\dot{m}_{O_2,4}}\right)_{st}$, which corresponds to the ratio of the flow mass rate of fuel over the oxygen flow mass rate divided by the same ratio at stoichiometric condition. An ER of 1 corresponds to stoichiometric mixture of fuel and oxygen. An ER smaller than one means that there is more oxidizer than necessary. The engine analysis is used to compute the average flow conditions at the exit of the combustor for the undeformed geometry. The aerodynamic solution and heat transfer equations are solved simultaneously. This analysis is referred to as conjugate heat transfer analysis (CHT). A conjugate heat transfer analysis is performed at a given flight condition, given the freestream and combustor conditions to predict the aerodynamic load and temperature distribution in the load carrying structure as function of time. Pressure and temperature are transferred to a structural finite element model (FEM) from which thermal elastic deformation of the vehicle airframe is obtained. The aerothermoelastic analysis is used to estimate the amplitude of maximum static deformations. The structural modeling of the hypersonic vehicle is simplified. The trajectory of the vehicle is assumed to be level flight. Because of these assumptions, the deformation are treated as uncertainties. An uncertainty propagation analysis is performed to evaluate the sensitivity of engine performance to the deformed configuration. Further details of each analysis is given in the following subsections.

A. Geometry

The geometry of the vehicle considered in this study is inspired by the X–43 depicted in Fig. 3. The (x, y, z) axis are attached to the body and respectively to the longitudinal, spanwise, and vertical directions respectively.

This generic geometry is representative of an airframe–integrated airbreathing scramjet propulsion system. The inlet is a slender wedge which compresses the freestream before it enters the isolator and the

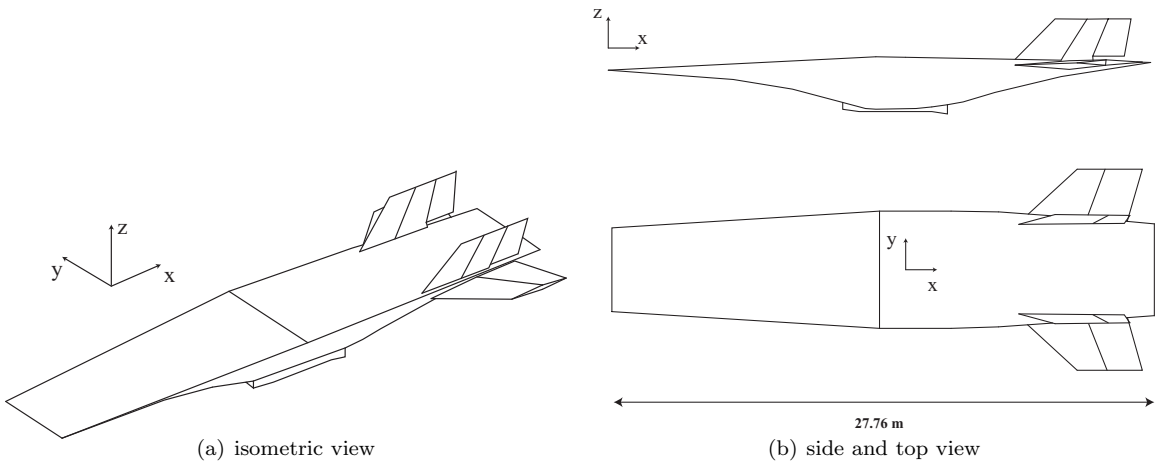

(a) isometric view (b) side and top view

Figure 3. Current vehicle geometry

combustor. The isolator prevents inlet unstart caused by the increase of pressure in the combustor. The combustor is the part of the engine where the fuel is injected and burns. The nozzle ensures expansion of the flow from the combustor conditions to the freestream conditions and generates thrust. The performance of the engine of this vehicle is estimated using a reduced–order model described next.

B. Propulsion System Analysis

Michigan AFRL Scramjet in Vehicle (MASIV) is an approximate, control–oriented model of the propulsion system of air–breathing Scramjet engines.[20,21] The geometry of the mean flowpath is depicted in Fig. 4. Each section corresponds to a component of the engine. Marching along the length of the vehicle, the propulsion system is divided into three components: the inlet and isolator, the combustor, and the nozzle. The points indicated in Fig. 4 define the geometry of the mean flowpath.

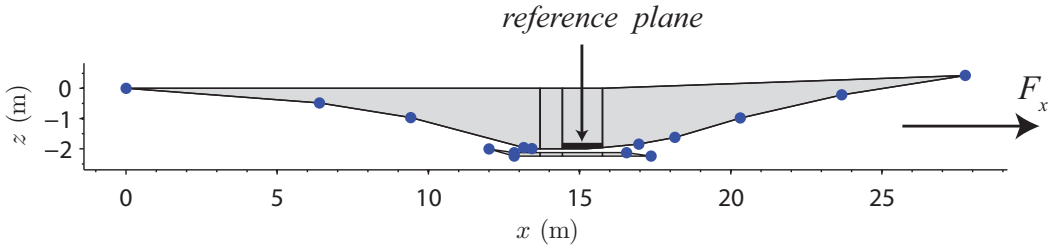

Figure 4. Engine flow path

This study focuses on the performance of the engine. The resultant of the pressure forces in the $x-$direction on the engine flowpath, F_x, is representative of the engine performance in generating trust which is the quantity of interest in this study. The number of points defining the compression ramp represents the number of compression shocks which compress the freestream before it enters the cowl. There are three compression shocks in the inlet ramp as illustrated in Fig. 4. The steady flow solution is calculated using the shock/expansion approach. Expansion fans are discretized into a finite number of 'expansion shocks'. Marching downstream, shock–shock and shock–discrete expansion fans interactions are solved by the solution of the local Riemann problem for perfect gas. Given a flight condition (altitude, H, Mach number, M_∞, and angle of attack, α), the mean flow properties at the entry of the engine in the isolator are predicted: density, static pressure, temperature and velocity. Mean flow properties at the entrance of the engine are computed and fed to the engine model. Enthalpy tables of a calorifically imperfect gas are used to account for high temperature effect at the entrance of the engine. In a calorically imperfect gas model, the specific heat c_p

and c_v of the fluid vary with temperature due to the excitation of vibrational energy of the molecules of gas.[11] Consequently, $\gamma = \frac{c_p}{c_v}$ is also a function of temperature. A more accurate prediction of the combustor inflow properties is achieved with this correction. The same model as for the inlet is used for the nozzle. The engine model is described in Ref. 22. The combustor model is a one dimensional (1D) model that solves for conservation of mass, momentum, and energy using equation of state and additional algebraic equations marching axially through the combustion duct. An algebraic spreading model allows transverse jet mixing which is required to model engines which are mixing–limited. Steady Laminar Flamelet Model (SLFM) is an approximate combustion model which considers finite–rate chemistry. The chemistry model is expect to be valid for an equivalence ratio, ER, between 0.1 and 2. The MASIV code was recently used in a control study of a rigid hypersonic vehicle.[23] The effect of angle of attack and inflow rate on the forces acting on a full vehicle (lift, drag, net thrust and pitching moment) were evaluated and used in a trim analysis.

The mass flow of the fuel is assumed to be independent of the deformation and corresponds to the mass flow at the prescribed equivalence ratio for the undeformed engine. An alternative approach assumes that the amount of fuel depends on the oxidizer mass flow at the entrance of the engine to keep the ER constant at all time. In this case, the fuel mass flow is affected by the deformation. The effect of the deformation on engine performance is then amplified. If the capture area decreases due to deformation, the air mass flow rate decreases in the combustor, the engine generates less thrust. If the equivalence ratio is kept constant when the vehicle deforms, less fuel is injected and thrust decreases accordingly. The plane corresponding to the top wall of the combustor is the plane of reference for the deformation of the vehicle, indicated in back in Fig. 4. The points, indicated with markers in Fig. 4, allows the analysis of a deformed engine. These points are used to transfer the deformation from the aerothermostructural model to the engine analysis.

C. Structural Model

The structure of an air–breathing hypersonic vehicle is subjected to significant non-uniform aerodynamic heating and pressure loading. In the development of hypersonic vehicles, structural components and design has played a important role.[7,10,24–30] The structure experiences high temperature gradients and intense pressure and heat loading which can cause local buckling or flutter. These challenges require innovative solutions: new high temperature materials, thermal protection system (TPS), and possibly coated leading edges with active cooling. The maximum operating temperature of titanium-based alloys varies between 800 to 1300 K.[29,30] Those materials were studied for potential application in the NASP program. In Ref. 31, materials for structural components are titanium–aluminides and titanium matrix composites. The structural model is developed to estimate the longitudinal aerothermoelastic deformation of the airframe and cowl and identifying the main contributors to aerothermoelastic deflections. The problem of local buckling of the leading edges is not considered. Similarly issues related with aerothermoelasticity of the wings and control surfaces are not included in this model.

The MSC.NASTRAN structural model of the body is illustrated in Fig. 5. MSC.NASTRAN is a finite element solver widely used in the aerospace industry. The model of the vehicle contains 540 nodes, 3240 degrees of freedom , with 208 CQUAD4 shell elements which represent the skin of the vehicle and the primary load carrying structure. The interior of the vehicle is filled with 534 CHEXA solid elements to prevent breathing modes–type deformation of the structure.

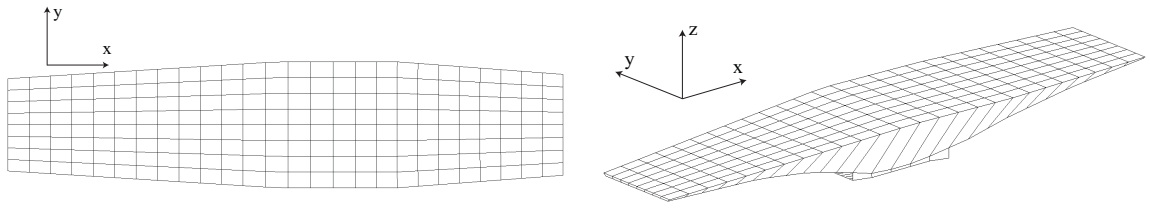

(a) top view (b) isometric

Figure 5. Structural Mesh

The skin is the load carrying structure represented by corrugated panels made of high temperature titanium alloy illustrated in Fig. 6 and presented in Ref. 32 as a potential load carrying structure for hypersonic vehicles. The model of the corrugated panel is used as a guideline for the longitudinal Young

modulus of the skin of the vehicle. The material properties assigned to the solid elements correspond to an orthotropic material with high stiffness in the (y, z) plane and low stiffness in the x–direction. This approach prevents unrealistic breathing modes and longitudinal deformations of the vehicle depend only on the skin properties. The vehicle behave similarly to a sandwich beam where cross sections remains planar. Material properties are functions of temperature.

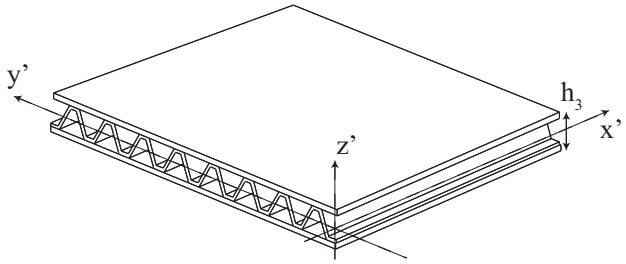

Figure 6. Truss–core sandwich panel[32]

The rigid body degrees of freedom are suppressed using the inertia relief option in MSC.Nastran. It allows one to compute the deformation of the structure with respect to a given point in its reference frame. The forces which result from a rigid body acceleration of the degrees of freedom at a prescribed node in the specified directions, referred to as "SUPORT", are calculated. Accelerations are applied to the structure in the "SUPORT" directions to balance the artificially applied loads. Free flight deformation can be computed. The computed solution is relative to any rigid body motion that is occurring. It was verified that deformation are independent of the choice of the support point where all degrees of freedom are constrained. The point at the center of the top wall of the combustor, in Fig. 4, is chosen as the reference point.

The nodal temperature and pressure are computed using a conjugate heat transfer analysis described next. There is no feedback mechanism to account for deformation in the aeroheating and heat transfer analysis.

D. Conjugate Heat Transfer Analysis

The solution of a structure heated by a fluid flow at one of its boundary is called conjugate heat transfer (CHT) problem. In this work, it is used to estimate the temperature distribution inside the undeformed load carrying structure of the vehicle as function of time and flight condition. Temperature distribution in the structure is calculated using CFD++, a commercial finite volume code capable of solving heat transfer problems in solid and conjugate heat transfer problems.[33] Using CFD++, the Navier–Stokes equations and the heat equation are solved simultaneously for the fluid and structure domain respectively. Heat flux is conserved through the fluid–TPS and TPS–structure interfaces. The gas model corresponds to calorifically imperfect gas: specific heat, c_p, is function of temperature, γ is not a constant. Turbulence is modeled using Goldberg turbulence model which is a single equation model for the undamped eddy viscosity, R_t, recommended for external turbulent hypersonics flows.[33]

To protect the load carrying structure from intense aerodynamic heating, a thermal protection system (TPS) barrier is placed between the airflow and the structure as depicted in Fig. 7. The TPS is composed of an upper layer of radiation shield made of PM2000 Honeycomb and a lower internal multiscreen insulation (IMI) barrier which is a simplified layout used in Refs. 34 and 27, which is shown to be a light and efficient TPS system.[35,36] IMI is also used in Ref. 26 as the main heat barrier for a long range hypersonic vehicle. The thicknesses of the TPS layers are uniform. An optimization analysis is often required in order to design the TPS distribution, such as performed in Ref. 26, and it was not performed in the present study.

The mesh for the fluid domain is depicted in Fig. 8. The thin skin structural layout is represented in Fig. 8(b). The leading edge of the vehicle experiences high aerodynamic heating. It is a critical component of the vehicle. However the emphasis of this study is on the body deformation. For this reason the leading edge is treated as an adiabatic wall in the CHT analysis. This assumption is also used for the cowl boundary. The combustor is the only part of the engine that is not represented. The MASIV model is used to estimate the flow conditions at the exit of the combustor. The entrance of the combustor is modeled by an outflow–only boundary condition. There is no back–pressure boundary condition in the analysis because the engine is

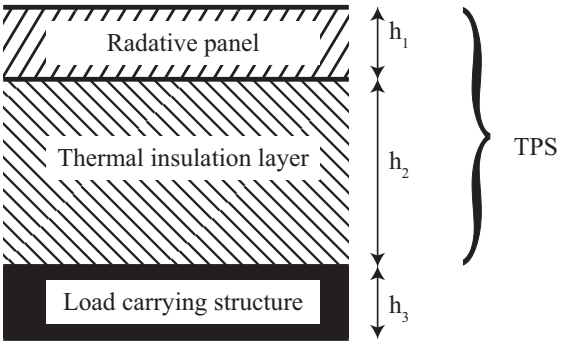

Figure 7. TPS layout

operating in SCRAM mode similarly to the assumption of MASIV analysis.

Pressure and temperature are linearly interpolated from the entrance of the combustor to the exit of the combustor and then transferred to the structural model. This approximation alleviates the high thermal and pressure loading that occurs in the combustor, a region that has the highest temperature and pressure on the vehicle. Further refinement of both aerodynamic and structural models are required so as to capture precisely the aerothermoelastic effects that occurs in the combustor. However, the modeling of these effects is outside the scope of the present study.

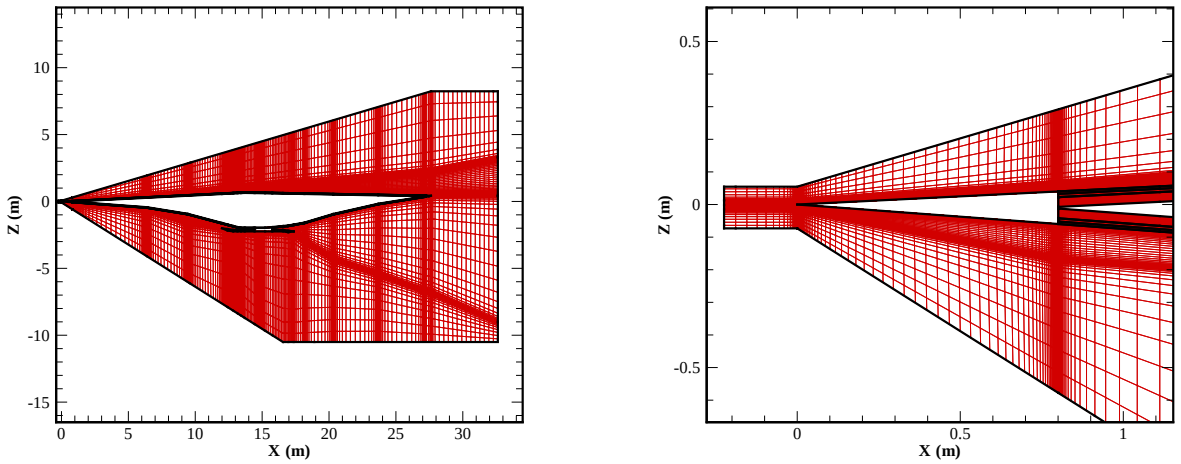

(a) Full mesh

(b) Leading edge view

Figure 8. CHT mesh

Transient temperature distributions in the structure are computed given by a flight trajectory characterized by a constant angle of attack, α_f. Pressure loading is calculated based on the angle of attack, α which maybe different of α_f, in the case of manoeuver for instance.

The deformation of the engine geometry in MASIV is given by Eq. 1, where $\bar{w}_{FEM,1}$ and $\bar{w}_{FEM,2}$ refer to the interpolated displacements from the FEM model for the vehicle and the cowl respectively at the (x, z) coordinates of the points which define the geometry of the flowpath shown in Fig. 4.

$$w_{MASIV,i}(x,z) = \xi_i \bar{w}_{FEM,i}\,(x,z;t,\alpha_f) \quad i = 1,\ 2 \tag{1}$$

The deformed shapes of the body of the vehicle, $\bar{w}_{FEM,1}\,(x,z;t,\alpha_f)$ and the cowl, $\bar{w}_{FEM,2}\,(x,z;t,\alpha_f)$

given by a flight history characterized by α_f and after a flight time t, are treated as maximum possible deformations of the vehicle. The amplitudes of the deformations of the vehicle and the cowl, ξ_1 and ξ_2 respectively, are treated as variables in an uncertainty propagation analysis for engine performance. The axial displacement, u, is treated the same way.

III. Uncertainty Propagation Analysis

Once the sources of uncertainty have been identified and quantified by appropriate probability distributions, the effect of uncertainty can be studied using two methods: intrusive and non-intrusive approaches.[37–39] The hypersonic propulsion problems require the use of non-intrusive methods due to their complexity. Based on a previous study on uncertainty propagation in aeroelastic and aerothermoelastic analyses,[19] stochastic collocation has been identified as the most cost effective alternative to direct Monte Carlo simulation and was selected for this study.

Direct Monte Carlo Simulations (MCS) requires numerous evaluations of the function of interest (e.g. F_x), at different values of the uncertain inputs, determined from their probability distribution. This method is guaranteed to converge to the correct probability distribution for the output of interest when the number of analysis runs is increased. Direct MCS can be applied to any output of interest, even when discontinuities are present.

The SC approach[18] is a computationally efficient polynomial response surfaces capable of approximating the relation between uncertain inputs ξ and the output of interest $f(\xi)$ when f is a continuous function of ξ. The expensive analysis, f, is evaluated at a given set of inputs (ξ_i), called collocation points. The polynomial response surface, given by Eq. 2, is generated using Lagrange polynomials associated with the collocation points, (ϕ_i), to interpolate the output of interest over the entire domain.

$$f(\xi) \simeq \hat{f}(\xi) = \sum_{j=1,N_I} f(\xi_j)\phi_j(\xi) \tag{2}$$

For the one dimensional case, the polynomial response surface, given by Eq. 2, is generated using Lagrange polynomials $(\phi_j)_{j=1,P+1}$, associated with the collocations points $(\xi_k)_{k=1,N_I}$, Eq. 3.

$$\phi_j(\xi) = \prod_{k=1,k\neq j}^{N_I} \frac{\xi - \xi_k}{\xi_j - \xi_k} \quad j = 1, P+1 \tag{3}$$

Lagrange polynomial are equal to 1 at their particular collocation point and 0 at all other points, Eq 4. This property ensures that the value of the response surface is exact at the collocation points.

$$\phi_j(\xi_k) = \delta_{jk} \quad k = 1, N_I \quad j = 1, P+1 \tag{4}$$

The degree of the polynomial approximation P, in Eqs. 3 and 4 is equal to $N_I - 1$. For a multidimensional random input space, $\boldsymbol{\xi} = (\xi^{i_v})_{i_v=1,N_v}$, in which N_v is the number of uncertain inputs, the multi-variate extension of Eq. 3 is given by Eq. 5.

$$\phi_j(\boldsymbol{\xi}) = \prod_{i_v=1}^{N_v} \prod_{k=1,k\neq j}^{N_I} \frac{\xi^{i_v} - \xi_k^{i_v}}{\xi_j^{i_v} - \xi_k^{i_v}} \quad j = 1, P+1 \tag{5}$$

For uniform probability distribution, the numerical integration evaluation is computed using Gaussian quadrature.[40] For a single random variable, the numerical integrations points are the roots of the Legendre polynomial function of degree N_I. The numerical integration scheme is exact for polynomial functions of order less than $2N_I - 1$. The collocation points are chosen such that mean, m_f, and variance, σ_f^2, are numerically estimated using a numerical integration scheme defined by N_I points, ξ_j, and their respective weights, w_j, Eqs. 6 and 7 .

$$m_f = \int_\Omega f(\xi)p(\xi)d\xi \simeq \sum_{j=1,N_I} w_j f(\xi_j) \tag{6}$$

$$\sigma_f^2 = \int_\Omega \left(f(\xi) - m_f\right)^2 p(\xi)d\xi \simeq \sum_{i=1,N_I} w_i f(\xi_i)^2 - m_f^2 \tag{7}$$

There is strong evidence that SC approach has outperforms polynomial chaos expansion,[18] another widely used technique. Therefore SC is selected for this study. Note however that this method suffers from the curse of dimensionality which implies that increasing the number of random inputs increases exponentially the number of analysis runs and the computational cost of the method. The number of analyses required for the implementation of the SC approach is $(P+1)^{N_v}$. Furthermore, the collocation points associated with most integration schemes are located strictly within the domain of the input variable: extrapolation is required for response surface evaluations close to the domain boundaries which may adversely affect accuracy. Therefore, the set of collocation points is extended with the boundary of the interval of each variable as illustrated in Fig 9(a). When those additional points at the boundary are used, the method is referred to as SC extended (SCE). Other efficient interpolation techniques can be employed to create the response surface such as adaptive sparse grid interpolation,[41,42] Kriging surrogates[43] or multi-variable splines[44,45] if discontinuities are present.

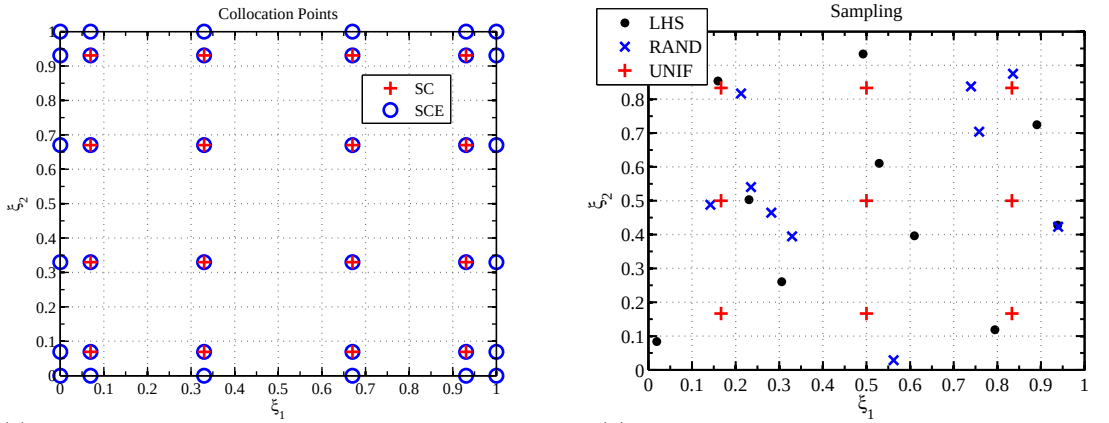

(a) Collocation points for uniform PDF for ξ_1 and ξ_2 (b) Sampling points for uniform PDF for ξ_1 and ξ_2

Figure 9. Illustration of different sampling approaches for two random variables ξ_1 and ξ_2 in $[0,1]^2$,

Once constructed, MCS can be applied on the computationally inexpensive polynomial response surfaces to obtain the probability distributions associated with the output of interest, this process is referred to as indirect MCS (IMCS). Latin hypercube sampling (LHS) method is used to perform the statistical analysis. The LHS is usually employed for space filling sampling which is equivalent of uniform probability density function (PDF). In Fig. 9(b), each cell of the grid has the same probability of 1/100. The LHS explores the uncertain variables space more efficiently than a cartesian grid (UNIF) and sampling points do not cluster as much as for random number generator (RAND) as illustrated in Fig. 9(b).

The efficient uncertainty analysis accounts for approximations in the calculation of the displacement. Transferring the deformation as random variables is effective for mitigating the effect of approximations and facilitates the introduction of uncertainty at an early stage in the design.

IV. Results

The vehicle is assumed to be 27.8 meters long, this length has been chosen based on the work done on NASP and Hyper–X programs as well as previous concepts.[7,9,46,47] In Ref. 21, the performance of two different flowpath geometries of the system inlet–combustor–nozzle are compared. The first configuration is optimized for a single flight condition being $M_\infty = 8$, $H = 26014.5\ m$ and $\alpha = 0^o$. The second configuration is designed to be less sensitive to changes in freestream Mach number and angle of attack.[21] Both geometries yield three compression shocks in the inlet ramp and two compression turns in the cowl. The more robust geometry contains an additional turn at the shoulder of the inlet which defines the entrance of the internal inlet. This geometry is the one used in this study, as observed in Fig. 4.

The flight condition used in this study corresponds to Mach 8 at an altitude of 26 km (80 000 ft) with 0^o angle of attack (AoA) which corresponds to the average design condition of the inlet.[20] The freestream condition is given in Table. 1. Using the MASIV code, the average flow condition at the exit of the combustor,

given in Table. 2 are obtained. The conditions are employed at the exit of the combustor in the CHT analysis.

Table 1. Freestream conditions

Parameter		Value	Unit
Angle of attack	α	rad	0
Altitude	H	m	26000
Mach number	M_∞	-	8
Static pressure	p_∞	Pa	2183.8
Temperature	T_∞	K	222.5588
Stagnation temperature	$T_{0,\infty}$	K	3071.3
Density	ρ_∞	$kg.m^{-3}$	0.0342
Reynolds number	$Re_{,\infty}$	m^{-1}	5.6245×10^6
Dynamic pressure	q_∞	Pa	98000 (2000 psf)

Table 2. Combustor conditions

Parameter		Value	Unit
Mach number	M_4	1.95	-
Static pressure	p_4	3.5742 10^5	Pa
Temperature	T_4	2039.0	K
Stagnation temperature	$T_{0,4}$	3584.7	K
Density	ρ_4	0.47	$kg.m^{-3}$

A. Conjugate Heat Transfer

The thermal properties and thicknesses of the TPS layers are given in Table. 3.

Table 3. TPS material properties

		PM 2000	IMI	Structure
Thickness	h_i (m)	0.0074	.01	0.03
Density	ρ_M (kg/m^{-3})	7196.567	72.864	4306
Emissivity	ϵ	0.75	–	–
Thermal Conductivity	k $(W/m/K)$	18.25	0.0582	21.9
Specific Heat	c $(J/kg/K)$	770	107	540

The CHT results are depicted in Figs. 10(a), 10(b), 10(c), and 10(d) which shows respectively temperature, pressure, Mach and γ contours around the vehicle. At the upper surface, the flow experiences a compressive shock at the leading edge followed by an expansion after the second edge downstream as observed in Figs. 10(a), 10(b), and 10(c). At the lower surface, the freestream experiences three compression shocks due to the lower surface of the inlet before it reaches the leading edge of the cowl and enters the internal inlet and isolator where a series of shock occurs. At the nozzle, the flow expands creating propulsive force for the vehicle. In the internal inlet and expansion fan as well as boundary layers, the static temperature of the fluid is much higher and γ is reduced to 1.3 as observed in Fig. 10(d). This illustrates the importance of high temperature modeling for such regions.

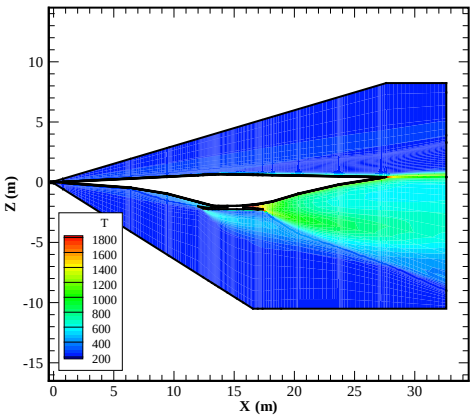

(a) Temperature (K)

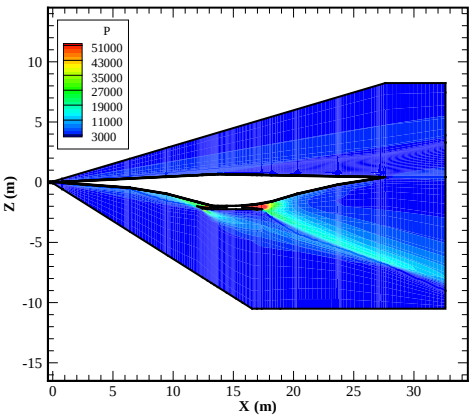

(b) Pressure (Pa)

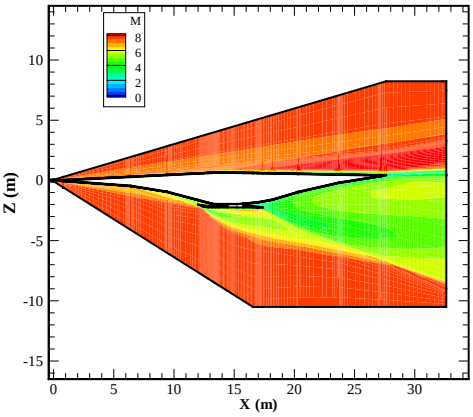

(c) Mach

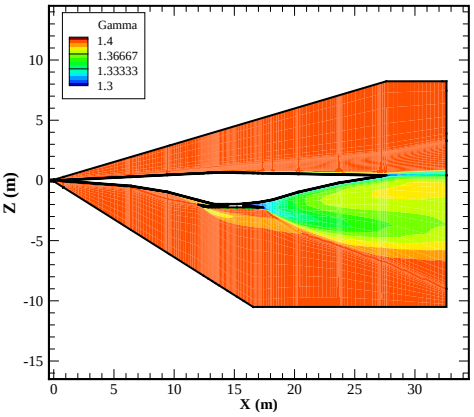

(d) γ

Figure 10. CHT results

The temperature at the lower surface of the skin as function of time is shown in Fig. 11. During flight, the load carrying structure heats up through the TPS. The aerodynamic heating rate is higher at the lower surface of the vehicle. Consequently the temperature rise is more important at the lower surface. Note that most of the vehicle remains at a temperature lower than 800 K for the first hour of flight. The central part of the engine: internal inlet, isolator, and internal nozzle experience the highest temperatures and may require additional thermal protection system or active cooling. The exact structural layout or cooling technology for those components is currently not well defined.

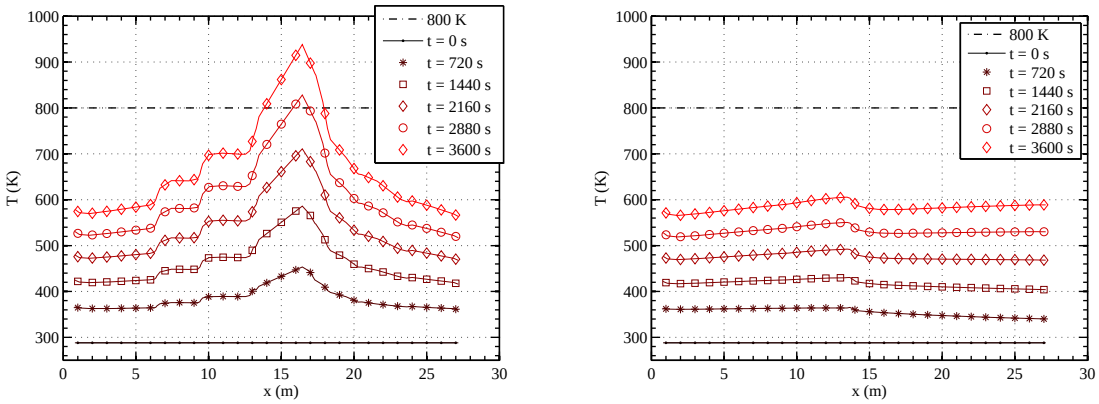

(a) Upper skin (b) Lower skin

Figure 11. Temperature in the skin as a function of time, $\alpha_f = 0^o$, $ER = 1.0$

The temperature distribution across the thickness of the vehicle is depicted in Fig. 12 and it corresponds to four different stations of the vehicle skin. These stations corresponds to the location of the first compression turn in the inlet ramp, Fig. 12(c), and the last compression turn in the nozzle, Fig. 12(d), and their equivalent on the upper surface of the vehicle, Figs 12(a) and 12(b) respectively. The temperature in the thin structure is considered uniform across the thickness compared to the variation in the longitudinal direction.

Temperature is linearly interpolated from the CHT results to the structural model as illustrated in Fig. 13(a) where the squares represent information pertaining to the FEM model and the lines results given by the CHT model for both upper and lower surface of the vehicle body. The two dimensional (2D) CHT model is used to compute the 2D loads on the three dimensional (3D) FEM model. The nodal pressures applied at each node are calculated based on their longitudinal coordinate, x, such that the total pressure applied along the center line of the vehicle is conserved. In Fig. 13(b), the nodal pressure is represented with square–shaped markers. In order to conserve pressure loading, the pressure at the nodes may be different than the linearly interpolated value. As a first approximation, the pressure on the side of the vehicle is interpolated from the upper surface to the lower surface. The leading edges and trailing edges of the vehicle are assumed to be rigid and are not modelled in the FEM model. However, the resultant aerodynamic forces and moments on the leading edges and trailing edges computed in the CHT model are applied as distributed forces at the respective leading edge and trailing edge of the vehicle FEM to conserve total force from the CHT model to the FEM model.

B. Aerothermoelastic Deflections

The skin of the vehicle is represented by an equivalent panel with homogenized properties[32] given in Table 4. Comparing the specific modulus i.e. the ratio $\frac{E}{\rho_M}$, the panel represents a lighter structure for comparable stiffness requirements. The thickness of top and bottom sheets is 1.5 mm. The corrugated sheet, in Fig. 6, obtained from superplastical forming and diffusion binding process, is 0.75 mm. The total thickness of the panel, h_3, is 0.03 m. The leading edges are assumed to be perfectly rigid. The upper surface of the internal inlet, isolator, combustor and internal nozzle is assumed to be made of titanium alloys. The high stiffness associated with this structural component of the airframe where the engine is mounted coincides with the highest thermal and pressure loads.

The total mass of the vehicle is 43 tons. For comparison purposes, the SR–71 was 32.74 meters long and

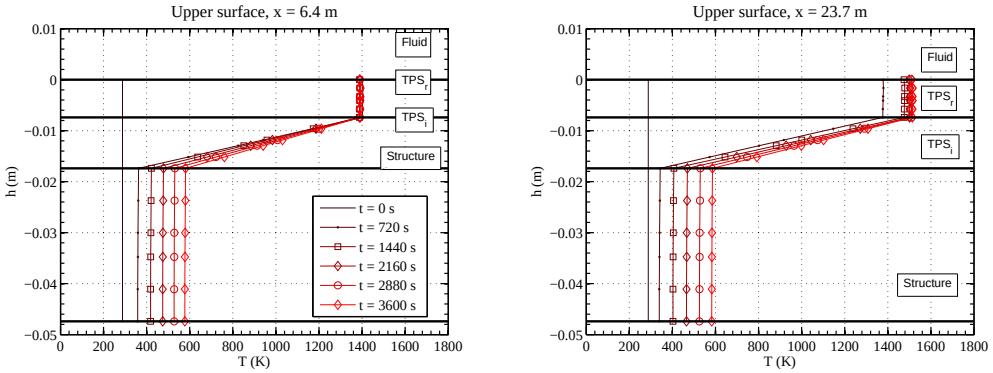

(a) upper skin, $x = 6.4m$

(b) upper skin, $x = 23.7m$

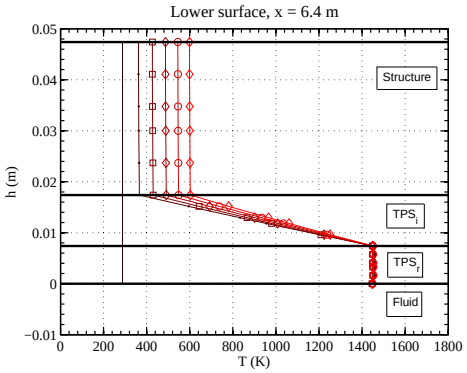

(c) lower skin, $x = 6.4m$

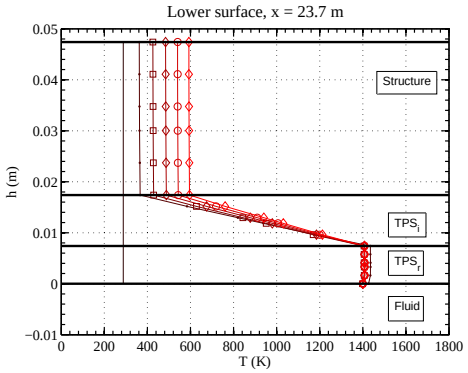

(d) lower skin, $x = 23.7m$

Figure 12. Temperature across skin thickness, $h = 0$ corresponds to TPS / freestream interface

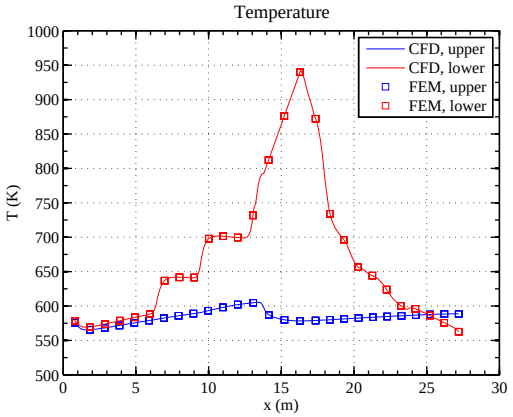

(a) Temperature

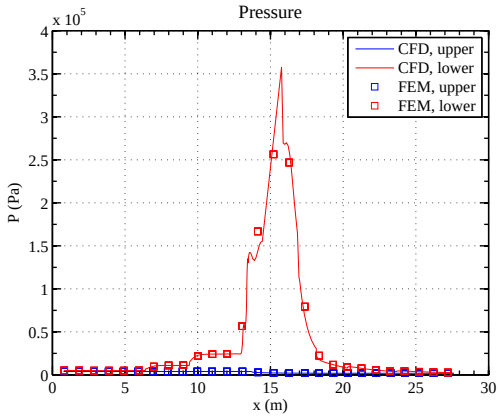

(b) Pressure

Figure 13. CHT and structural coupling, $\alpha_f = 0^o$, $t = 1h$, $ER = 1.0$

Table 4. Panel Properties

Titanium alloy	Density	ρ_M	$kg.m^{-3}$	4306
	Young Modulus	E	Pa	112×10^9
	Thermal expansion	α_T	K^{-1}	7.74×10^{-6}
	Poisson ratio	ν		0.3
	Specific modulus	$\frac{E}{\rho_M}$		2.6×10^7
Titanium alloy panel	Longitudinal flexural stiffness	D_x	Nm	6.2×10^4
	Thickness	h_3	m	0.03
	Density	ρ_M	kg/m^3	737.2
	Young modulus	$\bar{E} = \frac{12D_{x'}(1-\nu^2)}{h^3}$	Pa	32×10^9
	Specific modulus	$\frac{E}{\rho_M}$		4.3×10^7

its empty weight and maximum takeoff weight were 30 and 78 tons respectively. The natural modes shape of the vehicle are shown in Fig. 14. The first two and fourth elastic modes correspond to the first longitudinal bending modes having a natural frequency of 12.3, 19.2 and 26.7 Hz respectively. The third mode at 25.9 Hz is a lateral bending mode. The fifth mode is the first torsional mode at natural frequency of 28.2 Hz.

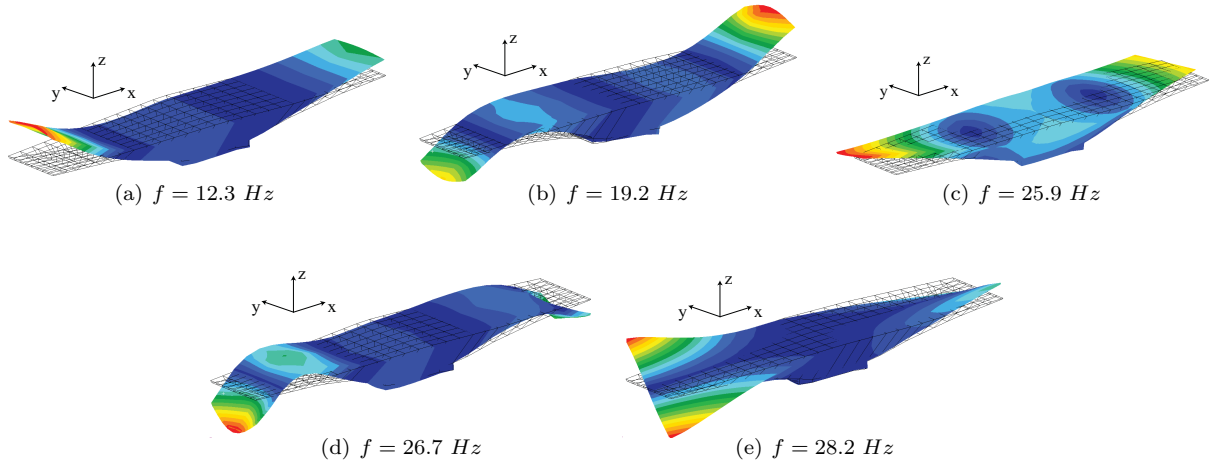

(a) $f = 12.3\ Hz$ (b) $f = 19.2\ Hz$ (c) $f = 25.9\ Hz$

(d) $f = 26.7\ Hz$ (e) $f = 28.2\ Hz$

Figure 14. First 5 natural mode shapes

The young modulus of the titanium alloy varies linearly with temperature from 100% to 70% at 288 and 810 K respectively. The coefficient of thermal expansion varies from to $7.74 \times 10^{-6}\ K^{-1}$to $9.54 \times 10^{-6}\ K^{-1}$ at 288 and 810 K respectively. These values are representative of a high temperature titanium alloy such as Ti–6Al–2Sn–4Zr–2Mo.[48] The initial temperature for the thermal expansion of the structure is set to 288 K which is the sea level temperature in a standard atmosphere model.

The temperature contours on the lower surface of the FE model of the vehicle are shown in Fig. 15 and corresponds to the temperature shown in Fig. 13(a). The highest temperature, 950 K, corresponds to the exit of the combustor. The lowest temperature at the upper surface is less than 600 K.

Similarly, pressure contours on the lower surface of the FEM are shown in Fig. 16 and correspond to the pressure shown in Fig. 13(b). As expected, temperature and pressure are dependent only on the $x-$coordinate on the lower surface. The variation along the spanwise direction is due to the interpolation from the elements of the lateral skin comprising the sides of the vehicle.

The vehicle is flying in a straight and level trajectory at constant altitude and Mach number. The angle of attack is constant and assumed to be $\alpha_f = 0^o$. The temperature increases in the structure as function of

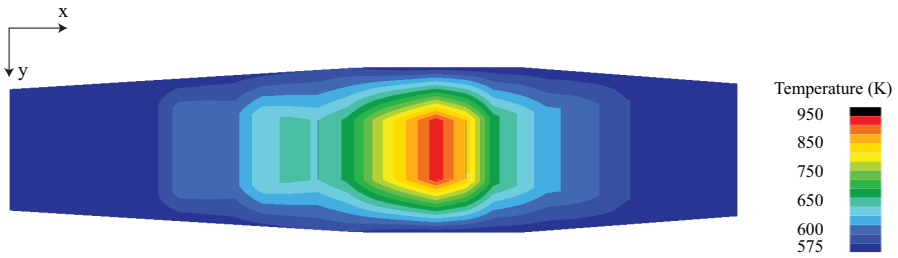

Figure 15. Temperature contours at the lower surface of the vehicle at $\alpha_f = 0^o$, $t = 1h$, $ER = 1.0$

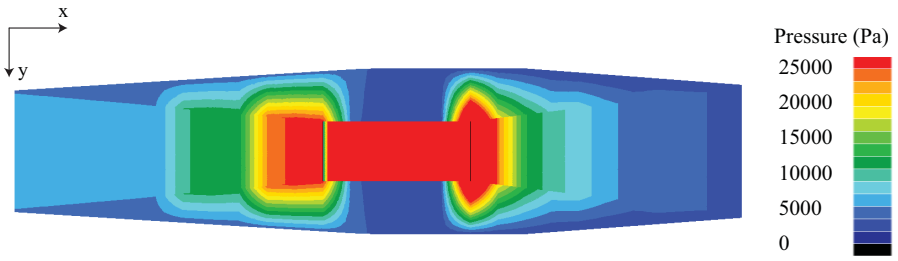

Figure 16. Pressure contours at $\alpha_f = 0^o$, $t = 1h$, $ER = 1.0$

time. As the structure heats up, material degradation and thermal stresses decrease the natural frequencies, shown in Fig. 17. The different bars in the figure correspond to different thermal loads. The variation in modal frequencies is of the order of 10% after an hour of flight at 0^o angle of attack. For a uniform temperature of 800 K, the variation in frequencies is of the order of -16% which corresponds primarily to material degradation.

The static deformations are computed at different times. The aerothermoelastic deformation of the vehicle along its plane of symmetry, $(y = 0)$, is shown in Fig. 18. The leading edge and trailing edge of the body deflects upward due to increasing temperature difference between the upper and lower surface at the inlet and nozzle respectively. After one hour of flight, the amplitude of the deflections is of the order of 8 cm which corresponds to 0.6% of the length of the inlet from the leading of the vehicle to the leading edge of the cowl. The deflections varies significantly with time: the aeroelastic deformation may be limited initially, but as the vehicle flies and heats up, material degradation and thermal stresses plays a significant role in deforming the vehicle. At the center line , the cowl deflects downwards due to high pressure loading at its upper surface. It is important to note that the cowl is modeled using a single shell element through the thickness. For this reason the temperature gradients which may occur between the upper and lower surface of the cowl are not accounted for. The temperature is assumed to be uniform across the thickness of the cowl. In an actual vehicle, similar to the inlet, the temperature at the upper surface of the cowl is higher than the temperature at the bottom of the cowl. However some active cooling design may alleviate part of the temperature difference through the thickness. In the model, the cowl structure has been assumed to be sufficiently flexible to account for potential deformations as a result of high pressure and thermal loading. Deflections of the order of 1.5 to 2 cm are obtained. It corresponds to approximately 0.9 % of the width of the engine. At the edge of the engine, the cowl is attached to the vehicle and its deformation follows the shape of the vehicle. The leading edge of the cowl deflects upwards. The amplitude of the deflection is of the order of -0.4 times the deflection at the center line at 0^o angle of attack. It dictates the range of the uncertain variable, ξ_2, in the uncertainty propagation analysis.

In Fig 19(a), the vehicle deformations are computed for different angles of attack from -1 ^{o} to 5 ^{o} at times $t = 720$ s and $t = 3600$ s. The temperature distribution in the structure is due to the flight time elapsed, while the pressure loading corresponds to the attitude of the vehicle at a particular time. In Fig 19(a), each

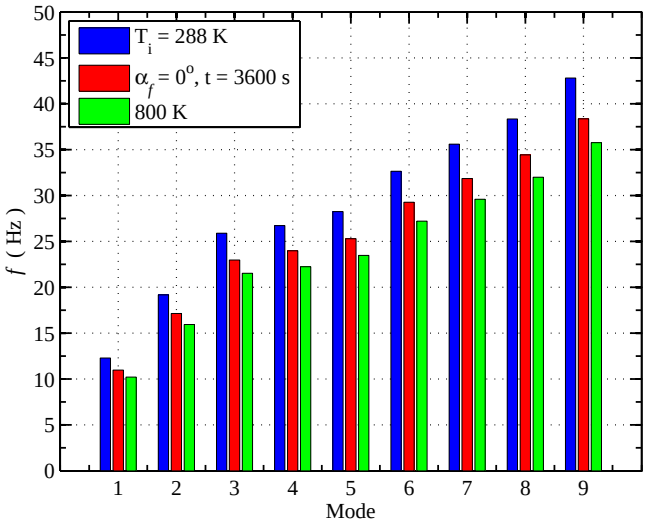

Figure 17. Structural layout concept

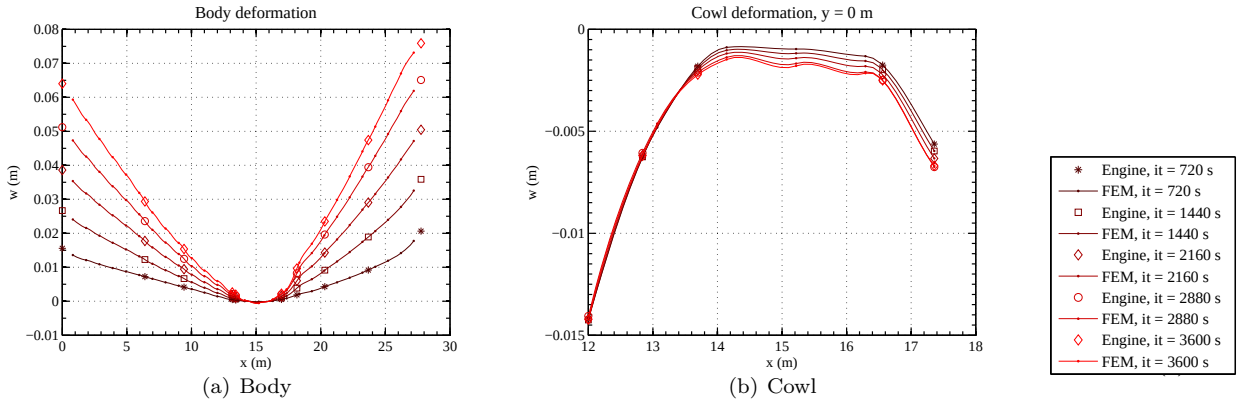

(a) Body (b) Cowl

Figure 18. FEM deformation as function of time along the centerline of the vehicle

deformation is due to a flight time of $t = 720\ s$ and $t = 3600\ s$ at $\alpha_f = 0^o$ angle of attack followed by a change of angle of attack which creates a different pressure loading on the heated vehicle. The results shows that the variation of the deformation with change in angle of attack is less than the one with change in flight time. It confirms the fact that aerothermoelastic effects have a greater effect on the deformation than the aeroelastic effects for the vehicle. In Fig. 19(b), for clarity, the results are shown for only $t = 3600\ s$. The deformations of the cowl do not depends significantly of the flight history. Its deformation depends primarily on aerodynamic loading since the cowl is not subject to temperature gradients across its thickness in this model.

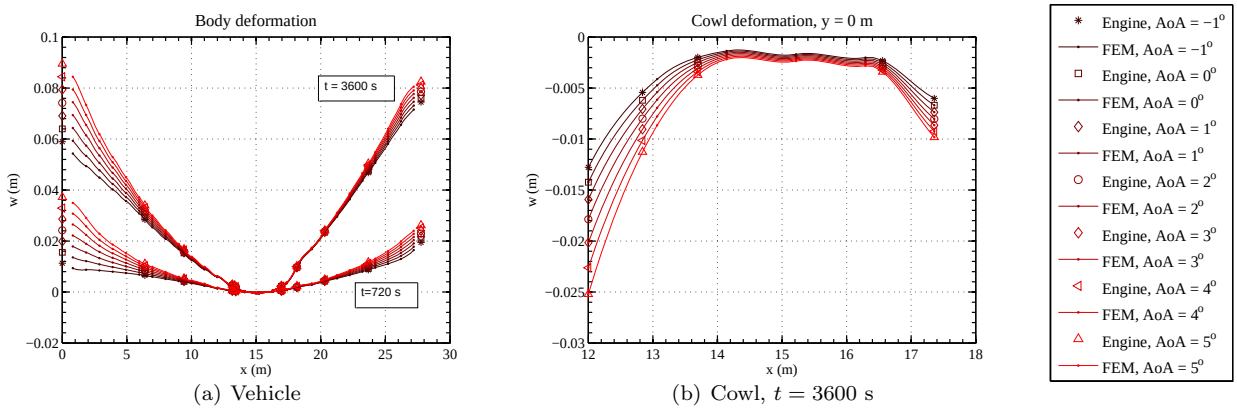

(a) Vehicle (b) Cowl, $t = 3600$ s

Figure 19. FEM deformation as function of angle of attack, $\alpha_f = 0^o$

In Table 5, the displacements at two different flight times and two different angles of attack are given. The axial deformation of the cowl leading edge are relatively small. The difference between the vertical displacements between the two trajectories is 16% at $t = 720$ s and 25% at $t = 3600$ s. The history of the flight as an increasing effect on the deformation of the vehicle.

Table 5. Displacements at the leading edges of the cowl and of the vehicle, $y = 0$

Flight history		$u\ (m)$	$w\ (m)$
$t = 720s$			
$\alpha_f = 0^o$	Vehicle	-0.0073	0.0156
	Cowl	-0.0039	-0.0142
$\alpha_f = 1^o$	Vehicle	-0.0073	0.0181
	Cowl	-0.0039	-0.0142
$t = 3600s$			
$\alpha_f = 0^o$	Vehicle	0.0114	0.0640
	Cowl	-0.0038	-0.0142
$\alpha_f = 1^o$	Vehicle	0.010	0.0803
	Cowl	-0.0044	-0.0142

Once the aerothermoelastic deflections have been studied, the uncertainty propagation analysis is performed for the two uncertain variables corresponding to the amplitude of the deformations.

C. Uncertainty Propagation Analysis

The uncertainties associated with thermal deflections of the vehicle and cowl were propagated through the analysis and their impact on the axial force, F_x are quantified. The 2D MASIV code predicts a force per unit length which is multiplied by the width of the cowl, 2.1 m, to give a force F_x in N. In Table 6, the

amplitude, ξ_1, of the deformation of the vehicle is assumed to vary between 0 and 1 and it corresponds to the deformation observed during the first hour of the flight. The amplitude of the deformation of the cowl, ξ_2, varies between -0.4 and 1 to cover the range of variation encountered during the first hour of flight and encompass the deformation shape which varies significantly from the centerline to the sides of the cowl where it is bonded to the vehicle.

Table 6. Displacement bounds and PDF for uncertainty propagation

	Variable	Lower Bound	Upper Bound	PDF
Vehicle deformation	ξ_1	0	1	uniform
Cowl deformation	ξ_2	-0.4	1	uniform

A convergence study is performed to determine the degree of the polynomial for the response surface which yields to an accurate approximate the analysis. A 5th order polynomial response surface was constructed based on $(5+1)^2 = 36$ analysis runs; i.e. 6 collocation points for the 2 random variables. Using this information, 50000 IMCS were performed on the polynomials response surface generated by SCE. The accuracy of the polynomial response surface is evaluated by comparing its prediction with the analysis at 77 uniformly–distributed reference points different from the collocation points. For this case, the maximum error is less than 0.8% of the deterministic value for all equivalence ratios and angles of attack for the 81 test points. Therefore the polynomial response surface is considered as a good approximation of the true function. Mean and standard deviation predicted by IMCS and numerical quadrature were identical within 0.7%.

The results of the uncertainty propagation study are shown in Fig. 20(a). The black line corresponds to the predicted axial force as a function of angle attack for two different equivalence ratios, $ER = 0.5$ and $ER = 1.0$. Examining the deformed configuration ($\xi_1 = 1$ and $\xi_2 = 1$) indicates that the performance of the engine is affected by the deformation. The vehicle deforming upwards and the cowl deforming downwards increase the magnitude of the axial force. This is due to the additional compression that occurs in the deformed inlet as well as an increased mass flow rate in the engine. In Fig. 20(a), the grey areas represent the full range of the axial force given the uncertainty in the deformation of the geometry. The change of performance is relatively small in magnitude and varies with the angle of attack from 4% to 28% of the value predicted for the undeformed configuration at $ER = 0.5$. The mean values are indicated with the dotted line. Error bars indicate the value of the mean plus or minus the standard deviation. The same deformation shapes obtained for Mach 8 are used to perform the same analysis of the engine performance but at a Mach number of 9. It indicates whether the same level of deformation have a different effect on the engine performance at another flight condition. The results are shown in Fig.20(b). This level of deformation have a comparable impact on the engine performance at Mach 9. This information can be useful in a design process to estimate the level of acceptable deformation.

In Fig. 21, the results of the uncertainty propagation analysis are normalized with respect to the value for the undeformed configuration and compared for two different trajectories. The first trajectory corresponds to a flight with one hour at $\alpha_f = 0^o$ angle of attack at Mach 8, and an altitude of 26 km. The second one corresponds to a flight angle of attack of $\alpha_f = 1^o$. The vertical deformation at the leading of the vehicle is 25% higher in the second case because of the additional increase of temperature due to the variation in this specific flight condition. The difference between both cases is relatively minor. The cowl deformations are almost equal in both cases, therefore it appears that the cowl is the main principal contributor to the effect on propulsion performance.

The output probability distribution extracted from IMCS results are shown in Figs. 22, which indicates that there is a significant probability that the magnitude of the axial force increases due to the deformation. In each figure, the horizontal axis shows the range of the axial force. The probability density function of the output (PDF), as represented by the bars, indicates the regions with higher probability. The cumulative density function, CDF(f), depicted with the curve, gives the probability that the output is smaller than the given value of the output $f(\xi)$: for instance, the probability that $\|F_x\|$ is less than the deterministic value is indicated by the markers in each figure.

The probability of failure, p_f is defined as the probability that the magnitude of the axial force is less than the deterministic value. Its value is calculated based on the IMCS results the CDF. It varies from a

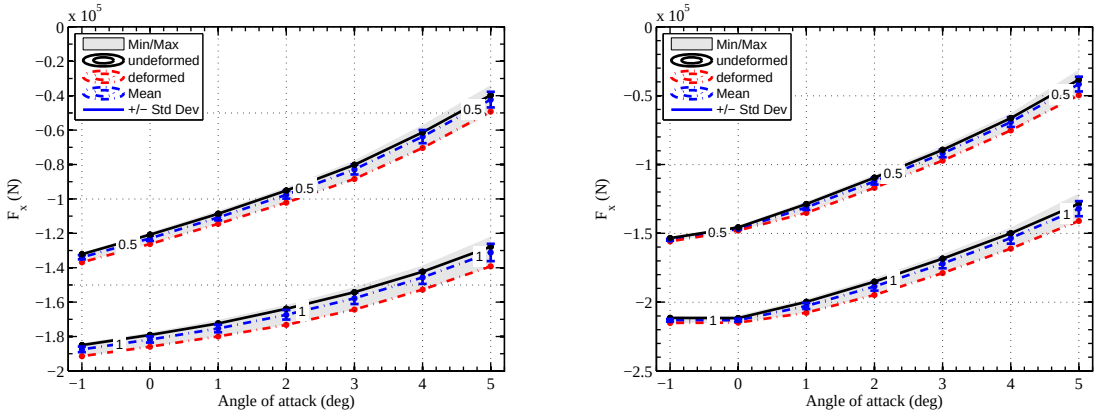

(a) Mach 8 (b) Mach 9

Figure 20. Uncertainty propagation results for $\alpha_f = 0^o$

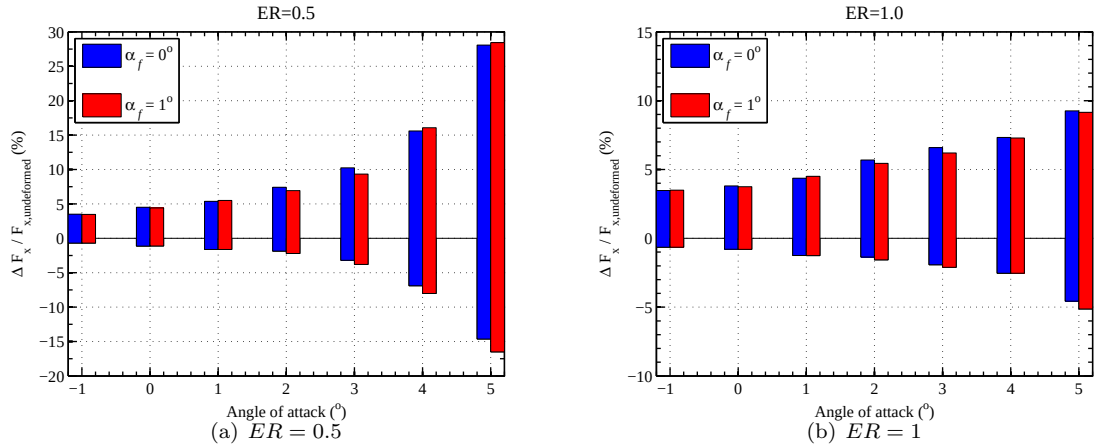

(a) $ER = 0.5$ (b) $ER = 1$

Figure 21. Comparison of uncertainty propagation results for two different trajectories, $M_\infty = 8$

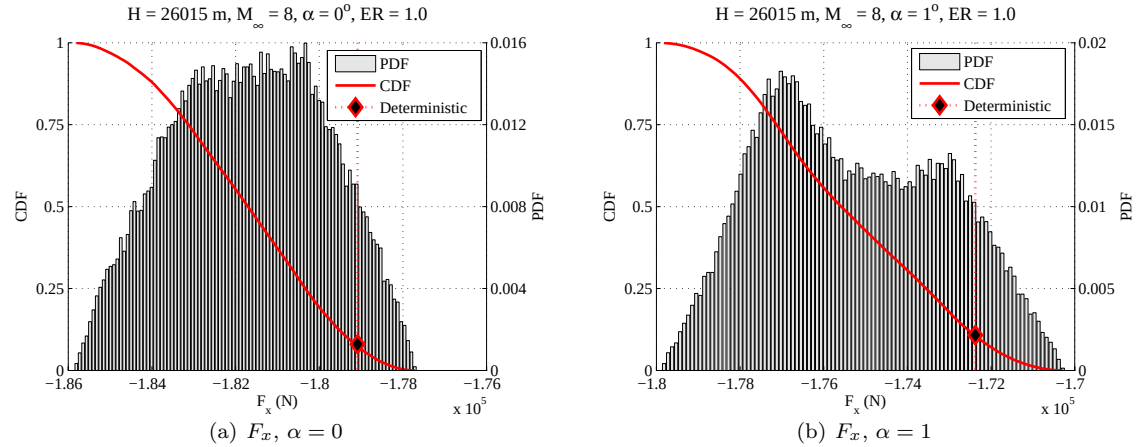

(a) F_x, $\alpha = 0$ (b) F_x, $\alpha = 1$

Figure 22. Uncertainty propagation results for Mach 8, $\alpha_f = 0^o$, $t = 1h$, $ER = 1$

few percent to 34% at 5^o angle of attack as illustrated in Fig. 23. These results clearly demonstrate the additional information which can be obtained by incorporating uncertainty in propulsion analysis problems.

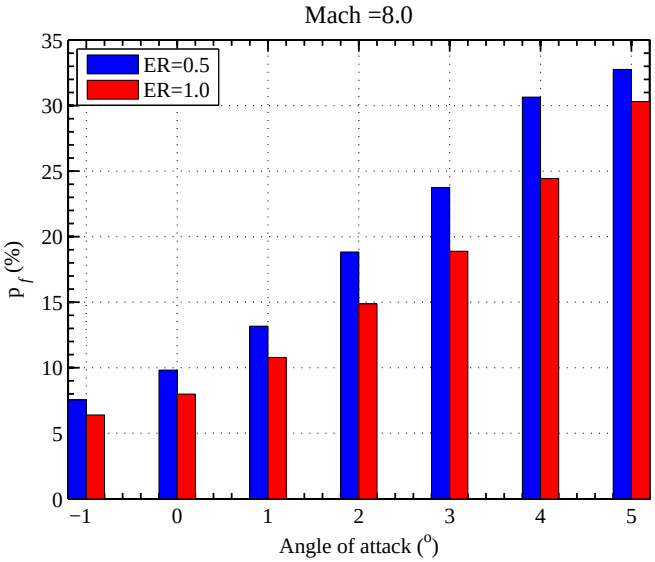

Figure 23. Probability of failure

To show the effect of keeping a constant equivalence ratio, ER, in the undeformed configuration, the same study is performed without prescribing constant fuel flow mass rate. Results shown in Figs. 24(a) and 24(b) indicate that there is a significant increase of the effect of deformation on the change in axial force for both Mach 8 and Mach 9. The variation range increases to up to 50% at an angle of attack of $\alpha = 5^o$ and $ER = 0.5$. In addition more fuel is injected in the combustor as illustrated in Fig 24(c). The range of the vehicle may decrease. In Fig. 24(d), the change in maximum pressure is depicted. The effect of deformation increases maximum pressure in the combustor which may affect significantly the chemistry of the combustion process. It is important to note that the reaction rates are interpolated from a database based on the local temperature. Currently the database is limited and its extension to a wider range of temperature is planned for the future.

V. Concluding Remarks

The results indicate that aerothermal deformations can be a source of uncertainty in airbreathing propulsion system modeling for hypersonic vehicles. Reduced–order models used in hypersonic aeroelastic and aerothermoelastic analyses based on insufficient knowledge associated with this class of problems require an uncertainty quantification approach.

1. The complexity of aerothermoelastic analyses requires expensive computations which are not suitable for control oriented models. However estimating aerothermoelastic deflections at an early stage of the analysis and propagating them through the propulsion analysis can alleviate the computational cost of the fully coupled analysis and provides a first step towards an improved understanding of this factor in airframe–integrated scramjet engine.

2. While the deformation due to the aerothermoelastic effects are relatively small deformation, these shed useful light on the understanding and quantification of the performance of the airframe–integrated engine for airbreathing hypersonic vehicles.

3. The cowl is identified as one of the most important contributors to both uncertainty and sensitivity of the propulsion system analysis. Accurate modeling of the thermal gradient through the main components of the structure is required. The structural model has to account for thermal gradient through the thickness of the main components as the vehicle airframe and cowl.

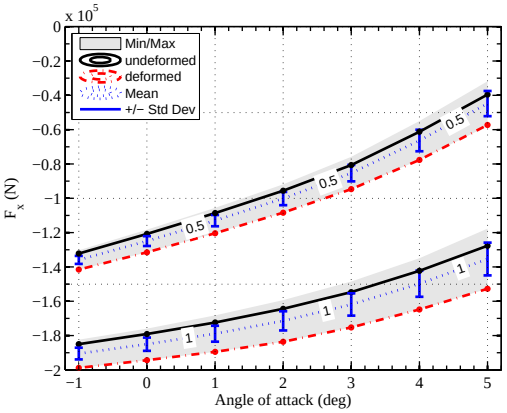

(a) F_x, Mach 8

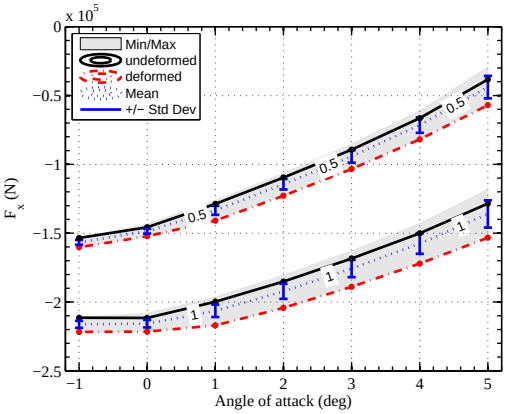

(b) F_x, Mach 9

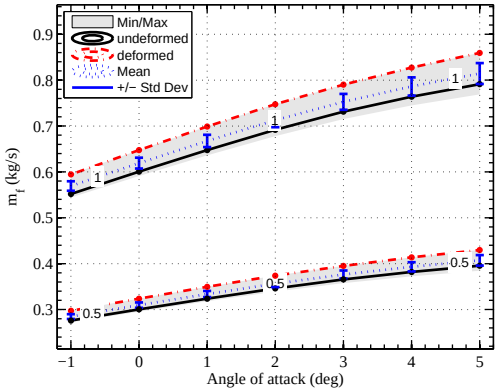

(c) Mach 8, Fuel flow mass rate, $\dot{m}_f$

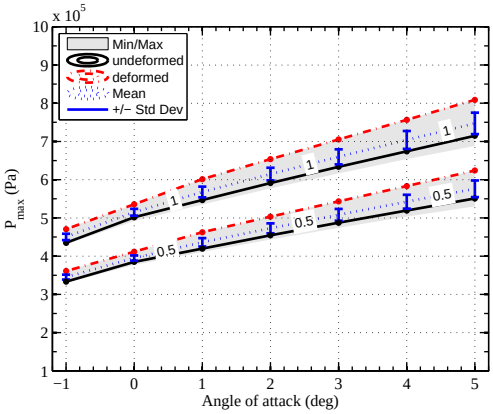

(d) Mach 8, Maximum Pressure in the combustor

Figure 24. Uncertainty propagation results for $\alpha_f = 1^o$, constant ER

4. Accurate modeling of the aerodynamic heating, flight history and control laws are required to fully understand the consequences of aerothermoelastic deformation on the overall performance of the vehicle throughout its mission.

Acknowledgements

This research is funded under NASA grant NNX08AB32A with Donald Soloway and Jorge Bardina as technical monitors. Support was also provided by AFRL grant FA 8650–07–2–3744 for MACCCS (Michigan AFRL Collaborative Center for Control Science), monitored by David Doman and Michael Bolender.

References

[1]McNamara, J. J. and Friedmann, P. P., "Aeroelastic and Aerothermoelastic Analysis of Hypersonic Vehicles: Current Status and Future Trends," *Proceeding for the 48th AIAA/ASME/ASCE/AHS/ASC Structures, Structural Dynamics, and Materials Conference*, Honolulu, Hawaii, April 2007, AIAA Paper No. 2007-2013.

[2]Fidan, B., Mirmirani, M., and Ioannou, P. A., "Flight Dynamics and Control of Air-Breathing Hypersonic Vehicles: Review and New Directions," *Proceedings of the 12th AIAA International Space Planes and Hypersonic Systems and Technologies*, Norfolk, Virginia, December 15–19 2003, AIAA Paper No. 2003-7081.

[3]Hallion, R. P., "The History of Hypersonics: or, Back to the Future - Again and Again," *Proceedings of the 43rd Aerospace Sciences Meeting and Exhibit*, Reno,Nevada, January 10–13 2005, AIAA Paper No. 2005-329.

[4]Dolvin, D. J., "Hypersonic International Flight Research and Experimentation (HIFiRE), Fundamental Sciences and Technology Development Strategy," *Proceedings of the 15th AIAA International Space Planes and Hypersonic System and Technologies Conference*, Dayton, Ohio, April 28 – May 1 2008, AIAA Paper No. 2008–2581.

[5]Voland, R., Huebner, L., and McClinton, C., "X-43A Hypersonic vehicle technology development," *Acta Astronautica*, Vol. 59, No. 1-5, 2006, pp. 181–191.

[6]Bertin, J. J. and Cummings, R. M., "Fifty years of hypersonics: where we've been, where we're going," *Progress in Aerospace Sciences*, Vol. 39, 2003, pp. 511–536.

[7]Rodriguez, A. A., Dickeson, J. J., Cifdaloz, O., Kelkar, A., Vogel, J. M., and Soloway, D., "Modeling and Control of Scramjet-Powered Hypersonic Vehicles: Challenges, Trends, and Tradeoffs," *Proceedings of AIAA Guidance, Navigation and Control Conference and Exhibit*, Honolulu, Hawaii, August 18–21 2008, AIAA Paper No. 2008-6793.

[8]Raney, D. L. and McMinn, J. D., "Impact of Aeroelastic–Propulsive Interactions on Flight Dynamics of a Hypersonic Vehicle," *Journal of Aircraft*, Vol. 32, No. 2, March–April 1995, pp. 355–362.

[9]Raney, D., McMinn, J., Pototzky, A., and Wooley, C., "Impact of aeroelasticity on propulsion and longitudinal flight dynamics of an air-breathing hypersonic vehicle," *Proceedings of the 34th AIAA/ASME/ASCE/AHS/ASC Structures, Structural Dynamics, and Materials Conference, 34th and AIAA/ASME Adaptive Structures Forum*, Vol. 1, April 19–22 1993, pp. 628–637.

[10]Bolender, M. A. and Doman, D. D., "Modeling Unsteady Heating Effects on the Structural Dynamics of a Hypersonic Vehicle," *Proceedings of the AIAA Atmospheric Flight Mechanics Conference and Exhibit*, Keystone, Colorado, August, 21–24 2006, AIAA Paper No. 2006-6646.

[11]Anderson, J. D., *Hypersonic and High Temperature Gas Dynamics*, Mc Graw Hill Editions, 1989.

[12]Bertin, J. J., *Hypersonic Aerothermodynamics*, AIAA Education Series, 1938.

[13]Dugundji, J. and Calligeros, J. M., "Similarity Laws for Aerothermoelastic Testing," *Journal of Aerospace Sciences*, Vol. 29, No. 8, August 1962, pp. 935–950.

[14]Smart, M. K., "Experimental Testing of a Hypersonic Inlet with Rectangular-to-Elliptical Shape Transition," *Journal of Propulsion and Power*, Vol. 17, No. 2, March–April 2001, pp. 276–283.

[15]Schulte, D., Henckels, A., and Neubacher, R., "Manipulation of SchockBoundary–Layer Interactions in Hypersonic Inlets," *Journal of Propulsion and Power*, Vol. 17, No. 3, May–June 2001, pp. 585–590.

[16]Schütte, G. and Staudacher, S., "Probabilistic Aspects of Scramjet Design," *Journal of Propulsion and Power*, Vol. 25, No. 2, March–April 2009, pp. 281–288.

[17]Chavez, F. R. and Schmidt, D. K., "Flight dynamics and control of elastic hypersonic vehicles - Modeling uncertainties," *Proceedings of AIAA Guidance, Navigation and Control Conference*, Scottsdale, AZ, Aug 1-3 1994, AIAA-1994-3629.

[18]Eldred, M. S. and Burkardt, J., "Comparison of Non-Intrusive Polynomials Chaos and Stochastic Collocation Methods for Uncertainty Quantification," *Proceedings of the 47th AIAA Aerospace Sciences Meeting Including The New Horizons Forum and Aerospace Exposition*, Orlando, Florida, January 5–8 2009, AIAA Paper No. 2009-976.

[19]

[20]Dalle, D. J., Fiota, M. L., and Driscoll, J. F., "Reduced–Order Modeling of Two–Dimensional Supersonic Flows with Applications to Scramjet Inlets," *AIAA Journal of Propulsion and Power*, Vol. 26, No. 3, 2009, pp. 545–555.

[21]Torrez, S. M., Driscoll, J. F., Dalle, D. J., and Fotia, M. L., "Preliminary Design Methodology for Hypersonic Engine Flowpaths," *Proceedings of the 16th AIAA/DLR/DGLR International Space Planes and Hypersonic Systems and Technologies Conference*, Bremen, Germany, October 19-22 2009, AIAA Paper No. 2009–7289.

[22]Torrez, S. M., Driscoll, J. F., Dalle, D. J., and Micka, D. J., "Scramjet Engine Model MASIV: Role of Mixing, Chemistry and Wave Interaction," *Proceedings of the 45th AIAA/ASME/SAE/ASEE Joint Propulsion Conference and Exhibit*, 2009, August 2-5 Denver, Colorado, AIAA Paper No. 2009-4939.

[23]Dalle, D. J., Frendreis, S., Driscoll, J. F., and Cesnik, C. E. S., "Hypersonic Vehicle Flight Dynamics with Coupled Aerodynamic and Reduced-Order Propulsive Models," .

[24]Bisplinghoff, R. L., "Some Structural and Aeroelastic Considerations of High-Speed Flight," *Journal of Aeronautical Sciences*, Vol. 23, pp. 289–330.

[25]Hunt, J. and Eiswirth, E., "NASAs Dual-Fuel Airbreathing Hypersonic Vehicle Study," *AIAA paper*, 1996, pp. 96–4591.

[26]Weirich, T. L., Fogarty, W., Dry, K., Iqbal, A., and Moses, P. L., "Dual-fuel Vehicle Airframe and Engine Structural Integration," *7th International Space Planes and Hypersonic Systems and Technologies Conference*, Norfolk, VA, Nov. 8-22 1996, AIAA Paper No. 1996-4594.

[27]Hunt, J., Laruelle, G., and Wagner, A., "Systems challenges for hypersonic vehicles," *Proceedings of the Future Aerospace Technology in the Service of the Alliance, AGARD Conference*, Vol. 3, Palaiseau, France, April 14–16 1997, NASA-TM-112908, AGARD-Paper-C37.

[28]Ko, W. L. and Gong, L., "Thermostructural Analysis of Unconventional Wing Structures of a Hyper-X Hypersonic Flight Research Vehicle for the Mach 7 Mission," Technical Report TP–2001–210398, NASA, 2001.

[29]Shih, P., Prunty, J., and Mueller, R., "Thermostructural concepts for hypervelocity vehicles," *Journal of Aircraft*, Vol. 28, 1991, pp. 337–345.

[30]Tenney, D., Lisagor, W., and Dixon, S., "Materials and Structures for Hypersonic Vehicles," *Journal of Aircraft*, 1989.

[31]Orton, G., Scuder, L., and Artus, J., "Airbreathing hypersonic aircraft and transatmospheric vehicles," *Future aeronautical and space systems*, 1997, pp. 297–371.

[32]Ko, W. L. and Jackson, R. H., "Combined Compressive and Shear Buckling Analysis of Hypersonic Aircraft Structural Sandwich Panels," Tech. rep., May 1991.

[33]Metacomp Technologies, Inc., *CFD++ User Manual - Version 8.1*, 2009.

[34]Culler, A. J., Crowell, A. R., and McNamara, J. J., "Studies on Fluid-Structural Coupling for Aerothermoelasticity in Hypersonic Flow," *Proceedings of the 50th AIAA/ASME/ASCE/AHS/ASC Structures, Structural Dynamics, and Materials Conference*, Palm Springs, CA, May 4–7 2009, AIAA Paper No. 2009-2364.

[35]Myers, D. E., Martin, C. J., and Blosser, M. L., "Parametric Weight Comparison of Current and Proposed Thermal Protection System (TPS) Concepts," *Proceedings of the 33rd Thermophysics Conference*, Norfolk, VA, 28 June – 1 July 1999, AIAA Paper No. 99–3459.

[36]Myers, D., Martin, C., and Blosser, M., "Parametric Weight Comparison of Advanced Metallic, Ceramic Tile, and Ceramic Blanket Thermal Protection Systems," Report NASA TM 2000–210289, National Aeronautics and Space Administration, June 2000.

[37]Murugan, S., Harursampath, D., and Ganguli, R., "Material Uncertainty Propagation in Helicopter Nonlinear Aeroelastic Response and Vibration Analysis," *AIAA Journal*, Vol. 46, No. 9, Sept. 2008, pp. 2332–2344.

[38]Pettit, C., "Uncertainty Quantification in Aeroelasticity: Recent Results and Research Challenges," *Journal of Aircraft*, Vol. 41, No. 5, September-October 2008, pp. 1217–1229.

[39]Hosder, S., Walters, R. W., and Balch, M., "Efficient Uncertainty Quantification Applied to the Aeroelastic Analysis of a Transonic Wing," *Proceedings of the 46th AIAA Aerospace Sciences Meeting and Exhibit*, Reno, Nevada, January 7-10 2008, AIAA Paper No. 2008-729.

[40]Golub, G. H. and Welsch, J. H., "Calculation of Gauss Quadrature Rules," Technical Report CS 81, School of Humanities and Sciences, Computer Sciences Department, Stanford University, November 3 1967.

[41]Klimke, A., *Sparse Grid Interpolation Toolbox User's Guide, v5.1*, Institute für Angewandte Analysis und Numerische Simulation (IANS), Universität Stuttgart, 2008, ISSN 1611-4176.

[42]Bunjgartz, H.-J. and Dirnstorfer, S., "Multivariate Quadrature on Sparse Grids," *Computing, Archives for Scientific Computing*, Vol. 71, No. 1, August 23 2003, pp. 84–114.

[43]Sacks, J., Welch, W. J., Mitchell, T. J., and Wynn, H. P., "Design and Analysis of Computer Experiments," *Statistical Science*, Vol. 4, No. 4, 1989, pp. 409–435.

[44]Jekabsons, G., *Adaptive Regression Splines toolbox for Matlab,ver. 1.3*, Institute of Applied Computer Systems, Riga Technical University, 2009, Reference manual.

[45]Friedman, J. H., "Multivariate Adaptive Regression Splines," *The Annals of Statistics*, Vol. 19, No. 1, March 1991, pp. 1–67.

[46]Bolender, M. and Doman, D., "Modeling unsteady heating effects on the structural dynamics of a hypersonic vehicle," *Proceedings of AIAA Atmospheric Flight Mechanics Conference and Exhibit*, 2006.

[47]Bolender, M. A. and Doman, D. D., "Nonlinear Longitudinal Dynamical Model of an Air-Breathing Hypersonic Vehicle," *Journal of Spacecraft and Rockets*, Vol. 44, No. 2, March–April 2007, pp. 374–387.

[48]Handbook-MIL-HDBK, "5H-Metallic Materials and Elements for Aerospace Vehicle Structures," *Knovel Interactive Edition-US Department of Defense*, , No. MIL-HDBK-5J, 31 January 2003.